The 2012 World Congress on
Advances in Civil, Environmental, and Materials Research (ACEM' 12)
Seoul, Korea, August 26-30, 2012

Segmentation of Multi-phase X-ray Computed Tomography Images of Porous Materials Considering Partial Volume Effect

*Masaji Kato[1)] and Hiroshi Yamanaka[2)]

[1)] *Faculty of Engineering, Hokkaido University, Sapporo, Hokkaido 060-8628, Japan*
[2)] *Graduate School of Engineering, Hokkaido University, Sapporo, Hokkaido 060-8628, Japan*
[1)] kato@geo-er.eng.hokudai.ac.jp

Manabu Takahashi[3)]

[3)] *Institute for geology and geoinformation, National Institute of Advanced Industrial Science and Technology, Tsukuba, Ibaragi 305-8567, Japan*

Satoru Kawasaki[4)] and Katsuhiko Kaneko[5)]

[4), 5)] *Faculty of Engineering, Hokkaido University, Sapporo, Hokkaido 060-8628, Japan*

ABSTRACT

X-ray computed tomography (CT) is a useful tool to visualize the internal features within non-transparent objects without destruction and also to offer us the quantitative information about the geometry and spatial distribution of each constituent forming the objects. However, X-ray CT images include blurs and noises to some extent. In this study, attention is paid to the partial volume effect causing the blurs depending on the resolution of the images. Artificial materials, such as packed glass beads and thin lines, and natural materials, such as oil sands, were observed using microfocus X-ray CT scanner. A maximum likelihood thresholding method that considered the partial volume effect was applied to the segmentation of two- or three-phase X-ray CT images. As a result, the porosities of the artificial materials and the proportion of liquid phase volume to total one of oil sands were quantitatively evaluated. Therefore, the segmentation method introduced in the study allows us to estimate the volume of each constituent forming porous materials with reasonable accuracy.

[1)] Assistant Professor
[2)] Graduate Student
[3)] Senior Researcher
[4)] Associate Professor
[5)] Professor

1. INTRODUCTION

X-ray CT can be used not only in the medical field but also in several occasions. For example, CT technique is useful in the case when non-destructive, non-disturbed observation is needed internal feature of multi-phase composites. From the standpoint of resources development engineering, we are trying to estimate internal structure of natural porous media such as oil sand and oil shale without destruction and disturbance. We dealt with segmentation of solid phase and fluid phase such as mineral and pore so far. However, we need to deal with three phase like solid, liquid, and gaseous phases. In this study, the method for two-phase segmentation considering partial volume effect is extended to three-phase segmentation and is applied to artificial materials such as metal wires and nylon threads for verification of this method and to natural material like oil sand.

Porosity, which is defined as the ratio of the pore volume to the total volume of the porous solid, is a physical property of porous materials and plays an important role in their mechanical and hydraulic behavior. Therefore, it can be an indicator of the mechanical and hydraulic properties of porous materials.

When measuring the porosity of porous materials, different approaches include weighing the materials and comparing their weights under dry and water-saturated conditions, mercury intrusion, or nitrogen gas adsorption porosimetry (Denoyel and Thommes, 2006). In addition, the pore area for a thin section of a sample can be observed under a microscope (Abell et al., 1999). As the samples will at minimum be cut, polished, heated, or immersed in fluid, the effect of the disturbance to the samples cannot be ignored.

In this study, we used X-ray computed tomography (CT), a nondestructive technique, to observe and analyze the internal structure of samples and estimate the porosity of porous materials. There is no well-defined standard for porosity estimation using CT images. Currently, researchers estimate the porosity through trial and error. This paper presents an automatic image segmentation technique for CT images of porous materials that considers the partial volume effect and its application to evaluating porosity and its variation in artificial and natural geologic materials.

2. SEGMENTATION METHOD

2.1 Mixel model considering partial volume effect

As mentioned in the previous section, the partial volume effect appears in digital images of multiphase materials without exception. Choi et al. (1991) introduced the concept of the mixel, or mixed pixel (voxel), to the classification of medical magnetic resonance images of brains. Numerous studies have focused on dealing with partial volume effects and/or mixels in medical science (e.g., Shattuck et al., 2001; Tohka et al., 2004; Kim et al., 2005), remote sensing (e.g., Okamoto and Fukuhara, 1996; Kageyama and Nishida, 2004), soil and rock engineering (e.g., Oh and Lindquist, 1999), and information technology (e.g., Kitamoto and Takagi, 1998a, 1998b, 1999, 2000). The mixel contains multiple constituents within a single pixel and then blurs the image to some extent. Conversely, pixels with only a single phase are called pure pixels.

Consider two-phase materials that are scanned by the X-ray CT scanner; consequently,

spatial distribution data of the X-ray attenuation coefficient are obtained. Grayscale images converted from the attenuation coefficient data are a mixture of pure pixels and mixels (Fig. 1). Each distribution of pure pixels is considered the normal distribution. The probability density function (PDF) of class i (corresponding to phase i) (i = 1, 2) within pure pixels can be expressed as follows:

$$f_i(x) = N\left(x; \mu_i, \sigma_i^2\right) = \frac{1}{\sqrt{2\pi\sigma_i^2}} \exp\left\{-\frac{(x-\mu_i)^2}{2\sigma_i^2}\right\} \quad \text{(i = 1, 2)} \qquad (1)$$

where $N\left(x; \mu_i, \sigma_i^2\right)$ denotes the normal distribution function with the intensity level x, expectation μi, and variance of class i. For mixels, the area proportion distribution is assumed to be an extension of the beta distribution; the PDF of mixels is given by the equation below (Kitamoto and Takagi, 1998b, 1999, 2000):

$$M(x) = \frac{1}{B(m,n)} \int_0^1 a^{m-1}(1-a)^{n-1} N\left(x; \mu_a, \sigma_a^2\right) da \qquad (2)$$

where the beta function is $B(m,n) = \int_0^1 a^{m-1}(1-a)^{n-1} da$ with the area proportion of constituent class 1, $0 \le a \le 1$, parameters m and n are greater than 0, and μ a and are as follows:

$$\mu_a = a\mu_1 + (1-a)\mu_2 \qquad (3)$$

$$\sigma_a^2 = a^2\sigma_1^2 + (1-a)^2\sigma_2^2 \qquad (4)$$

For simplicity, the parameters m and n in the beta function were set to 1 in the study under the assumption that the boundary of the two phases of a material is simple and smooth. The mixel class was assigned to class 3. An example of the distribution of two-class mixels is shown in Fig. 2. The intensity level histogram of the given image is the superposition of the normal distributions for pure pixels and mixels.

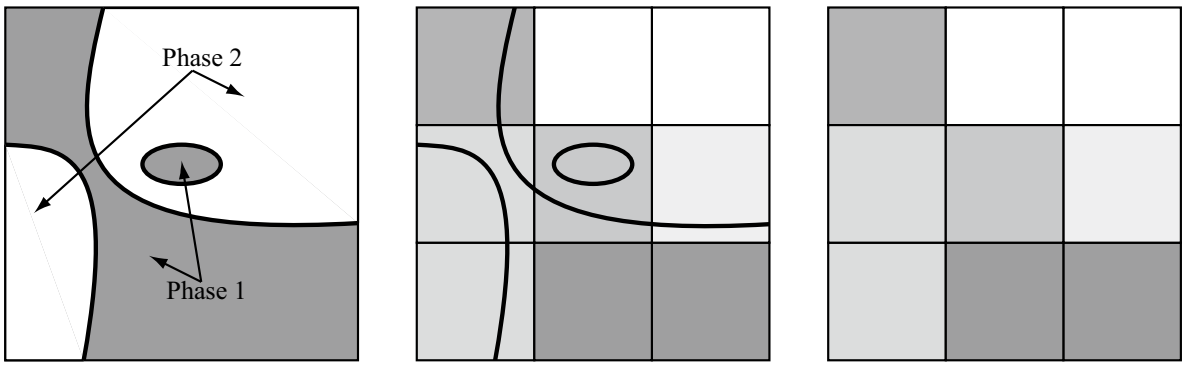

(a) (b) (c)

Fig. 1. Schematic of image acquisition. Grayscale digital images are made from two-phase substance due to quantization. (a) A real image and (b) and (c) its quantized images with partial volume effect, where boundary lines are remaining in (b).

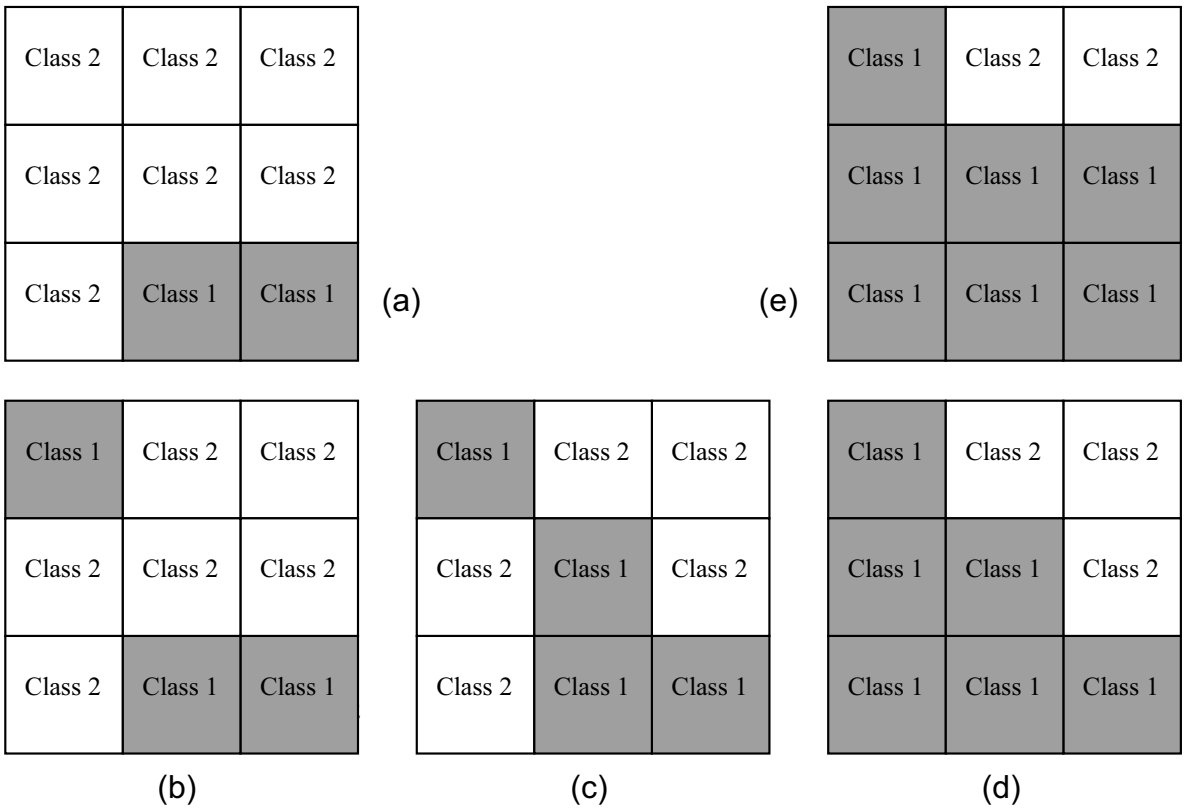

Fig. 2. Binarized images corresponding to Fig. 1. (a) Showing underestimated class 1 area and vice versa class 2 area, on the contrary (e) showing overestimated class 1 area and vice versa class 2 area, and from (b) to (d) intermediate ones.

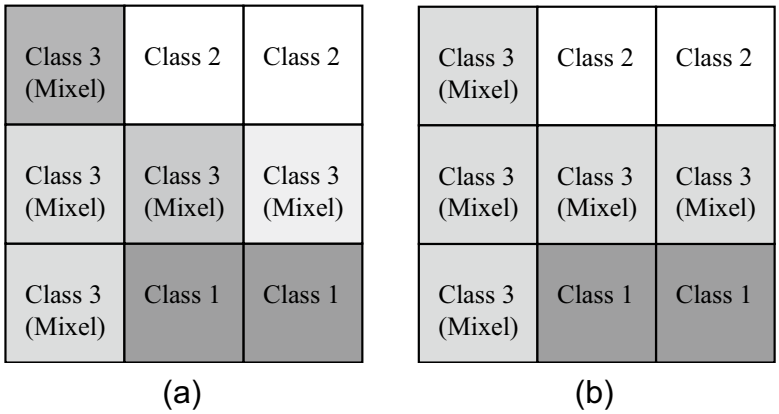

Fig. 3. Digital images corresponding to Fig. 1. (a) Original grayscale image and (b) image segmented with classes 1 and 2 representing pure pixels and class 3 representing their mixel.

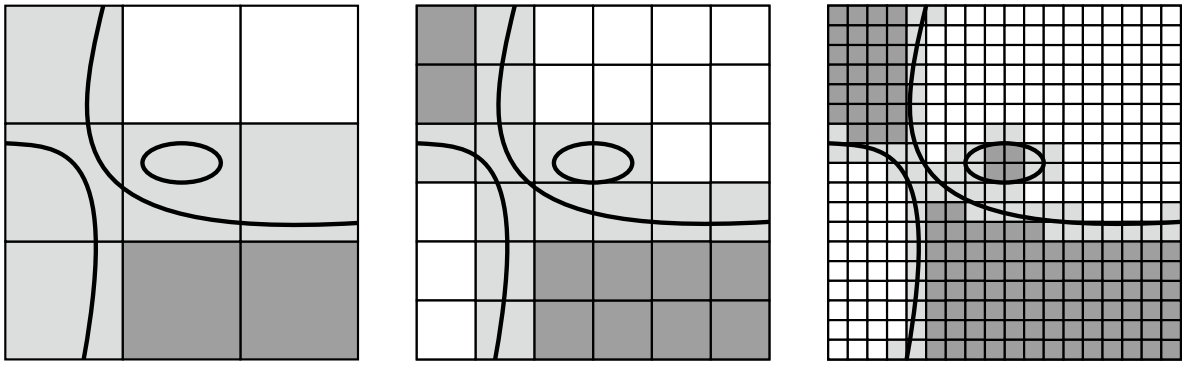

(a) (b) (c)

Fig. 4. Partial volume effect according to resolution of images. (a) Low resolution, (b) intermediate, and (c) high resolution.

2.2 Thresholding method

Numerous thresholding techniques have been developed by researchers (reviews in Sahoo et al., 1988; Pal and Pal, 1993; Sezgin and Sankur, 2004). However, the performance of each technique depends on the purpose and object. Baveye et al. (2010) reported difficulty in thresholding for soil images and X-ray CT data and its dependence on the observer.

Here, the scope was limited to two-class segmentation problems with a bimodal histogram obtained from digital images. Automatic image segmentation considering the effect of mixels was applied to the images. Kitamoto (1999, 2000) demonstrated the application of a mixel model to image classification of satellite images to separate the cloud phase from the sea phase. In this study, the maximum likelihood thresholding method proposed by Kitamoto (1999), which considers the effect of mixels, was used for two-class segmentation problems. The maximum likelihood thresholding criteria used in the study are listed in Table 1 (modified from Sekita et al., 1995) corresponding to the statistical properties of each class. In the table, k is the number of classes, M is the total number of classes, t is the threshold vector where the number of vector elements equals M − 1, and and are the occurrence probability and variance, respectively, of each class. An alternative notation is as follows:

$$\tilde{\sigma}^2 = \sum_{k=1}^{M} \tilde{\omega}_k \tilde{\sigma}_k^2 \qquad (5)$$

This equation denotes the expectation of each variance within a class. In this study, M was three (two for pure pixels and one for mixel); thus, the number of thresholds was two. The procedure for the selection of threshold values can be automated.

The expectation and variance of each class in the digital images were not clear beforehand. Accordingly, $J_K(\mathbf{t})$ should be selected first as the thresholding criterion. However, thresholding may lead to both thresholds being nearly equal. In this case, another criterion $J_D(\mathbf{t})$ should be tried next.

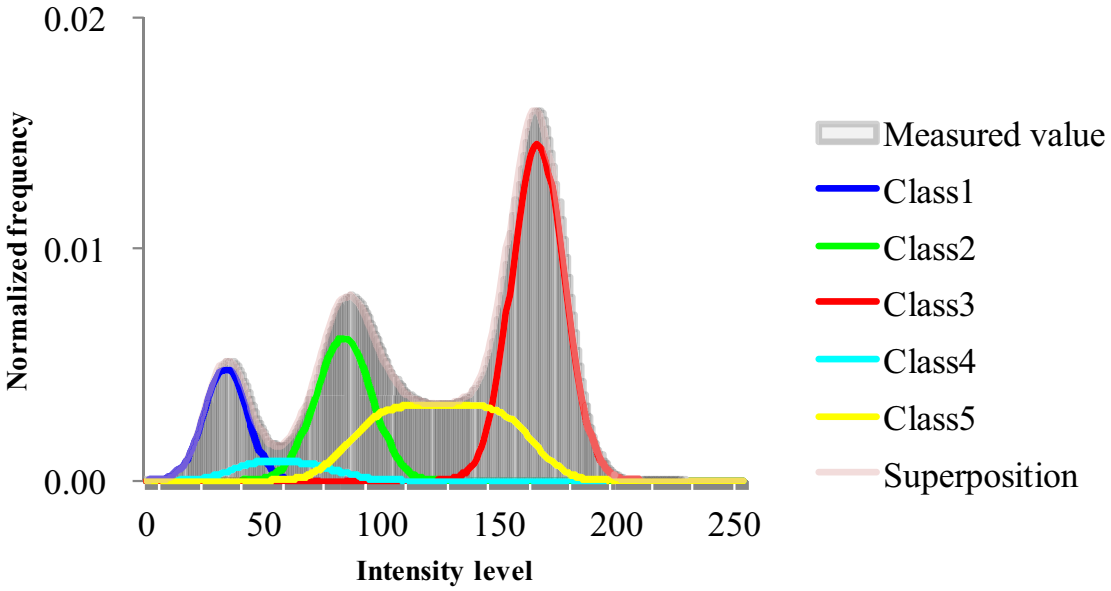

Fig. 5. Example of three-class mixel distribution. Lines show probability distributions of five classes and their superposition.

2.3 Porosity calculation

Once thresholds are decided, the porosity, which is the ratio of the pore volume to the total volume of the porous material, can be evaluated. We obtained the ratio of three classes (two classes for pure pixels and one class for mixel); however, this was not among the objectives of the study. At this point, we did not know what percentage of the mixels (pixels in class 3) belonged to each phase. To evaluate porosity, the area (volume) of mixels should finally be divided into two phases. It is reasonable that the area of mixels is divided into two phases by the ratio of the numbers of classes 1 and 2 (Kato et al., 2008; Kobayashi et al., 2009, 2010). Thus, the porosity of porous material is calculated using the following equation:

$$\phi = \frac{N_1}{N_1 + N_2} \tag{6}$$

where N1 and N2 are the numbers of pixels within classes 1 and 2, respectively. In this calculation, the number of mixels (pixels in class 3) does not appear.

3. X-RAY COMPUTED TOMOGRAPHY

3.1. Microfocus X-ray CT

X-ray CT is a non-destructive and non-invasive three-dimensional (3D) visualization and quantification tool. Microfocus X-ray CT is based on recording X-ray projections of the object at different angles and stacking several sequential slices. A filtered back-projection algorithm is then used to reconstruct a slice image through the object to

show the distribution of the linear attenuation coefficient. The attenuation coefficient depends on the applied X-ray energy and the atomic number and density of the object. Further descriptions of microfocus X-ray CT instruments and reconstruction algorithms are given by Kak and Slaney (1988).

This study used a microfocus X-ray CT scanner (TOSCANER 31300 μhd, Toshiba IT & Control Systems Co.) installed at Hokkaido University, Japan. This scanner has been used in several studies (e.g., Kawaragi et al., 2009; Kobayashi et al., 2009, 2010; Fukuda et al., 2010; Yamanaka et al., 2011). The focal spot size of the X-ray source assembly is 5 μm. Scans were made at 130 kV (maximum tube voltage of the device) and 62 μA, and the full-scan mode of a single slice was selected for this study. The voxel size was 5 μm $\times$ 5 μm in the cross-section and approximately 20 μm in height, and the matrix size was chosen to be 2048 $\times$ 2048 pixels. It is possible to arbitrarily set the number of views ($\leq$4800) and number of stacks per angle ($\leq$50). The distance between the focal spot of the X-ray source and center of the rotation (focus-center-distance; FCD) is also variable ($\leq$50 cm) and used to vary the resolution of the CT images.

The CT scanner must be calibrated before use to reduce artifacts and obtain clear images. In this study, the gain and position of the rotational center were carefully calibrated. However, the partial volume effect, which blurs material boundaries in images to some extent, was unavoidable because of the inherent resolution limitations of X-ray CT (Ketcham and Carlson, 2001). In this study, this effect was stochastically modeled and then explicitly used for image segmentation.

3.2. Samples

We used artificial materials and natural material. Artificial are aluminum wires and nylon threads.

4. RESULTS

4.1. Artificial materials

Metal wires and nylon threads

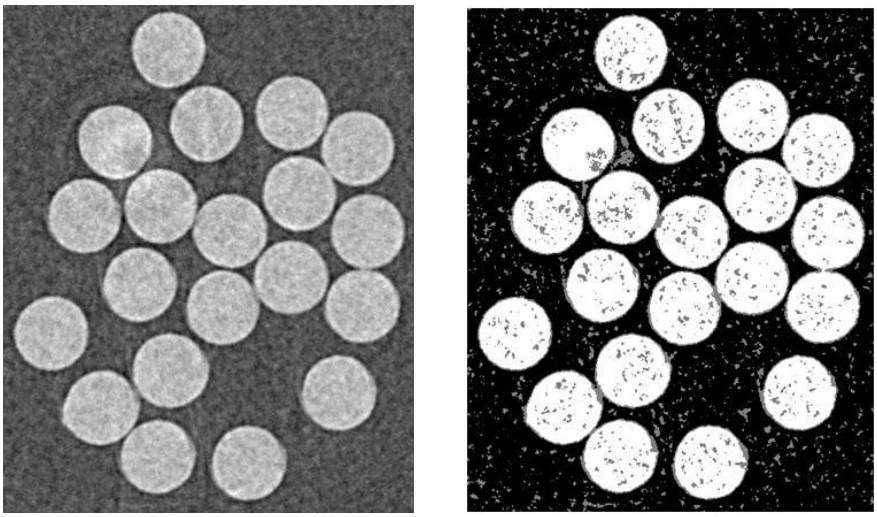

(a) (b)

Fig. 6. (a) Original X-ray CT image of only nylon threads (size 3.7 mm × 3.0 mm) and (b) image segmented using thresholding method based on mixel model; black regions represent class 1 (air), white regions represent class 2 (nylon threads), and gray regions represent class 3 (mixels).

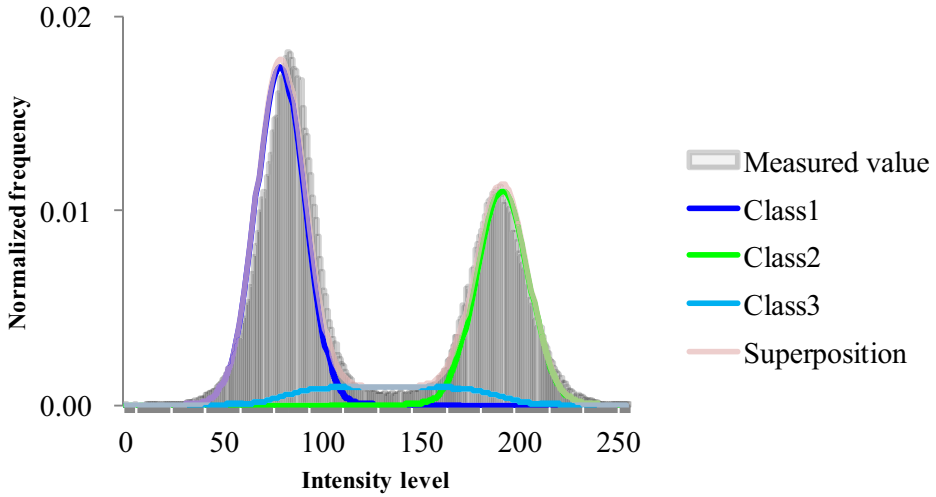

Fig. 7. Histogram of CT image of nylon threads in Fig. 6 (a). Lines show probability distributions of three classes and their superposition.

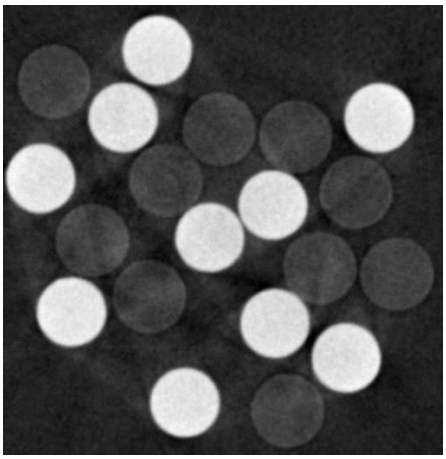

Fig. 8. Original X-ray CT image of nylon threads and aluminum wires (size 3.2 mm × 3.3 mm); black regions represent air, whereas white regions represent aluminum wires, and gray regions represent nylon threads.

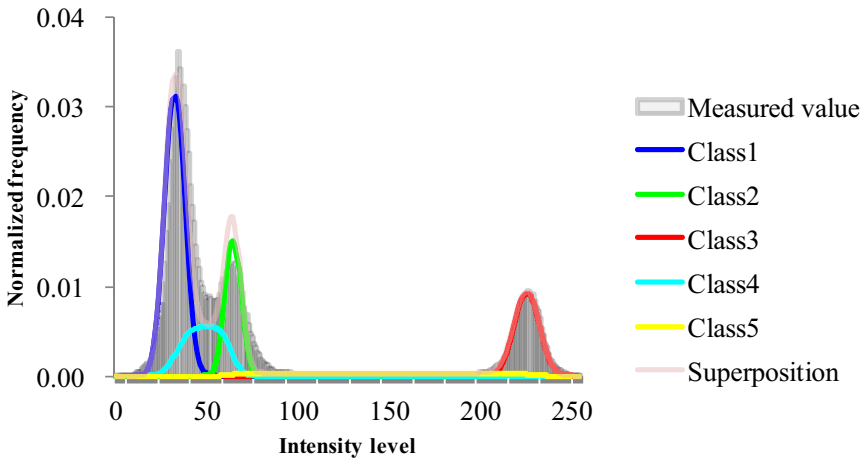

Fig. 9. Histogram of CT image of nylon threads and aluminum wires in Fig. 8. Lines show probability distributions of five classes and their superposition.

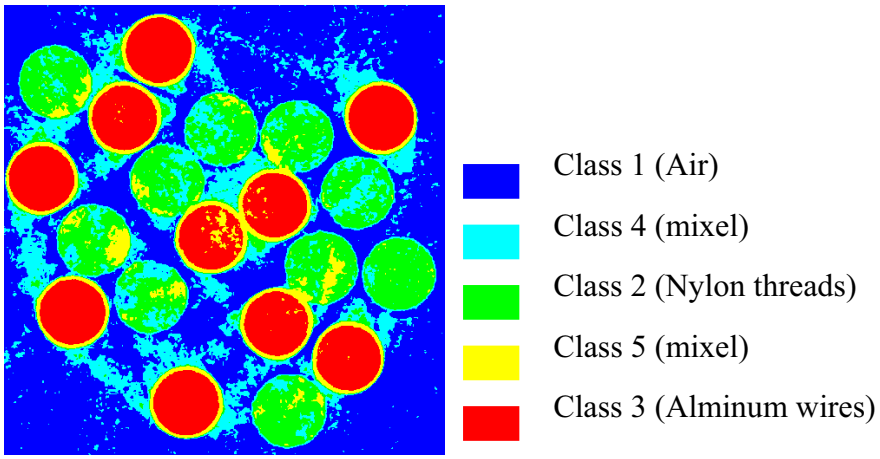

Fig. 10. Image segmented using thresholding method based on mixel model; blue regions represent class 1 (air), green regions represent class 2 (nylon threads), red regions represent class 3, sky blue regions represent class 4 (mixel between classes 1 and 2), and yellow regions represent class 5 (mixel between classes 2 and 3).

4.2. Natural materials

Oil sand

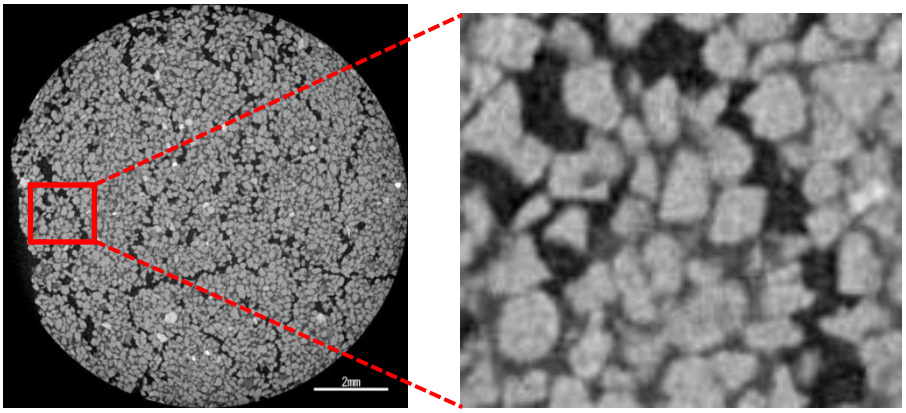

(a) (b)

Fig. 11. (a) Original X-ray CT image of oil sand and (b) enlarged view (size 1.4 mm × 1.6 mm); black regions represent air and light-gray regions represent sand grains.

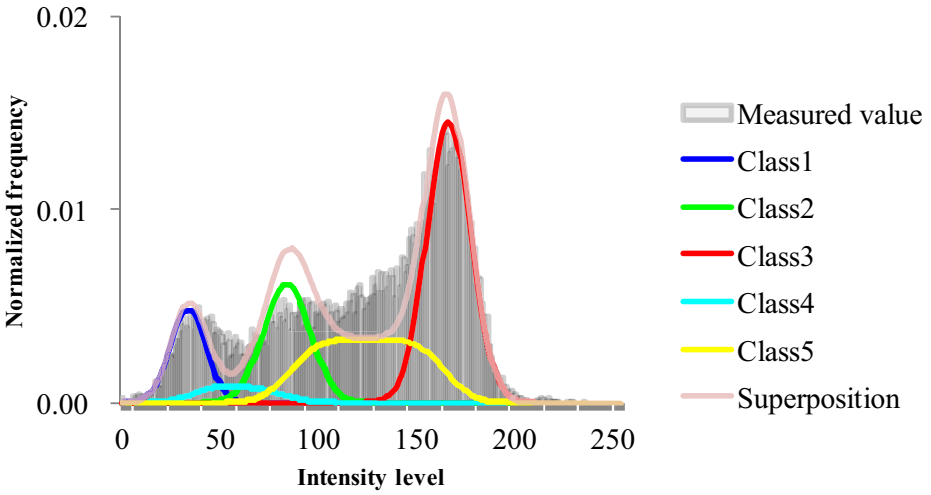

Fig. 12. Histogram of CT image of oil sand in Fig. 11 (b). Lines show probability distributions of five classes and their superposition.

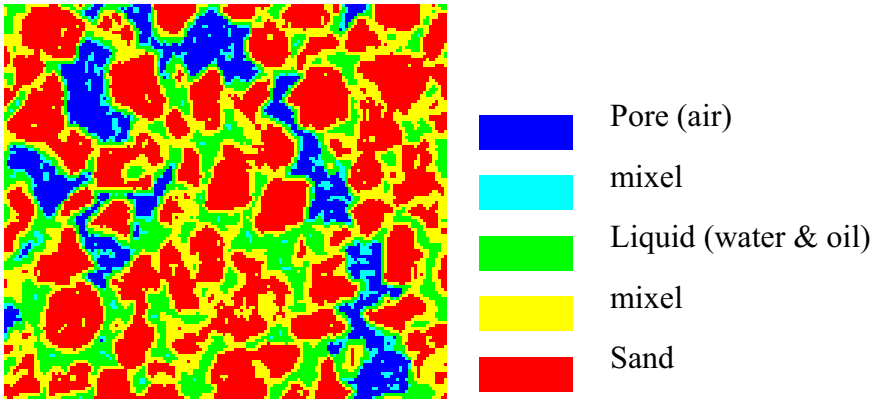

Fig. 13. Image segmented using thresholding method based on mixel model; blue regions represent class 1 (air in pore), green regions represent class 2 (liquid phase: water and oil), red regions represent class 3 (sand grains), sky blue regions represent class 4 (mixel between classes 1 and 2), and yellow regions represent class 5 (mixel between classes 2 and 3).

The thresholding method introduced in the previous section was applied to X-ray CT images of glass bead packing (i.e., an artificial material), and the porosity was evaluated. The effects of scanning conditions on the segmentation results were also examined.

Glass beads with a mean density of 2500 kg/m3 and mean particle diameter of 0.38 mm were gently placed into a polystyrene bottle with a 21.0 mm diameter and 54.8 mm height. This specimen was scanned using a microfocus X-ray CT scanner under various conditions, including the number of views (500–4800), number of stacks per angle (10–50), and FCD (100–260 mm). A grayscale image converted from the X-ray

attenuation coefficient is shown in Fig. 3. In the figure, the bright region represents the presence of a high-attenuation substance (i.e., glass beads in the specimen) and the dark region represents the opposite (i.e., voids in the specimen). Several particles of glass were white in color due to the heterogeneous glass bead density. When the effect of high density appears in the histogram, high-intensity data should be removed from the histogram during image analysis. Histograms of the CT images are shown in Fig. 4. In the figure, the frequencies of the three classes are drawn.

The porosities of this specimen under different conditions were evaluated using the porosity calculation equation mentioned in the previous section. The relation between the porosities of the glass beads and FCD (other scanning conditions were constant) is given in Table 2.

Porosity of oil sand

The same thresholding method was then applied to the X-ray CT images of Berea sandstone (i.e., a natural geomaterial), and its porosity was evaluated. Berea sandstone has been used in various studies on rock mechanics, and substantial scientific data have been collected (e.g., Lo et al., 1986; Zhang et al., 1990; Hart and Wong, 1995; Menéndez et al., 1996; Schembre and Kovscek, 2003; Takahashi et al., 2009).

A grayscale X-ray CT image of Berea sandstone is shown in Fig. 5. As in Fig. 3, the bright region represents a high-attenuation substance (i.e., mineral in the specimen), and the dark region represents the opposite (i.e., pores in the specimen). The histogram of the CT images is shown in Fig. 6. In the figure, the distance between the means of two classes is relatively small. This may lead to errors in the thresholded images. Fig. 7 shows logarithmic likelihood distributions corresponding to threshold vector t. The criterion of shown in Fig. 7(a) was adopted instead of and the threshold vector t was determined at maximum point. The criterion of shown in Fig. 7(b) was not suitable because both thresholds were nearly equal at maximum point. The frequencies of the three classes obtained from the histogram-based analysis are drawn in Fig. 6.

The porosity of this sandstone—as evaluated using equation (6) with the area occupancies of 0.153 in class 1 (pores), 0.679 in class 2 (minerals), and 0.168 in class 3 (mixel) —was 18.4 %. If half of the total mixel area is occupied by the pores in the specimen, the porosity is 23.7 %. Both values of porosity for the evaluated sandstone are listed in Table 3.

Estimation of porosity variation

In the previous sections, we evaluated the porosities of geomaterials. In this section, we focus on the variations in porosity within a porous material. Takahashi et al. (2009) quantified the pore geometry change of Berea sandstone with the increase of hydrostatic pressure. In this study, as given in Section 4.1, because of the ease of porosity measurement, the packing of glass beads was chosen from the choices of sands, glass beads, gum tips, plastic pellets, and steel balls.

The porosity of the specimen was changed using a biogrouting technique (Kawasaki et al., 2006). As summarized in Table 4, the specimens were prepared by mixing the grout solution for glass beads in a polystyrene bottle; this procedure is the same as that

described in Section 4.1. Although the use of the same specimen for both the grouted and ungrouted conditions is desirable, two different specimens were used to prevent yeast from being exterminated due to the first X-ray irradiation of the ungrouted specimen. The grouted specimen was made by mixing yeast into the specimen, which was then left to rest in an incubator at 25 °C. In contrast, the ungrouted specimen was not mixed.

The specimens were scanned using the CT scanner in the single slice mode and the resolution (voxel size) of the CT images was 5 μm × 5 μm × 16 μm. To enhance the reliability, 12 slices from each specimen were imaged. Fig. 8 shows example X-ray images of the grouted and ungrouted specimens. The white to light-gray regions represent glass beads, whereas the black to dark-gray regions represent the solution. Fig. 9 shows the histogram of the average X-ray attenuation coefficient from the 12 measured slices. The bell-shape distribution on the left side corresponding to the dark region indicates the solution, and the bell-shape distribution on the right side corresponding to the bright region indicates glass beads.

Pure pixels of the solution (dark gray) were assigned to class 1, pure pixels of glass beads (light gray) were assigned to class 2, and mixels were assigned to class 3. The area occupied by each class was calculated by integrating the frequency of each class using the estimated thresholds (Table 5). The porosity was calculated by substituting the calculated areas in Equation (6). Moreover, we calculated the average porosities of 12 slices of each of the grouted and ungrouted specimens (Table 5). The ratio of the average porosities of the grouted specimen to that of the ungrouted specimen was 0.98.

5. DISCUSSION

The average porosity of the packed glass beads that were gently placed in a bottle was 33.3%–36.7%, as shown in Table 2. The range of this value corresponded to the porosity between the tetragonal sphenoidal and cubical tetrahedral packing systems (e.g., Miwa, 1981). This is a reasonable result considering the glass bead packing process.

The porosity of Berea sandstone was 18.4% using the method in this study. The porosity of 23.7% calculated under a certain assumption may be an upper limit of the porosity. Therefore the value is given in parentheses in Table 3. The porosities of Berea sandstone were also measured using mercury intrusion porosimetry. Furthermore, the values in porosity of the sandstone have been given by Jaeger et al. (2007). These values are shown in Table 3 as well. When comparing the porosity calculated in the study with the other values, these values are in good agreement.

Shoji (2008) estimated the ratio of porosities of the biogrouted specimen to that of the ungrouted specimen by measuring the concentration of calcium ions and found the ratio to be 0.98–0.99. This is explained by the deposition of calcium carbonate on the surface of particles in the grouted specimen. Fig. 10 is a piece of evidence for the deposition of calcium carbonate on the grain surfaces and between the grains in the grouted sands. As shown in section 4.3, these two values are in good agreement. Thus, the method using X-ray CT and the maximum likelihood thresholding method considering the effect of mixels enables us to evaluate the change in porosity with high accuracy. Moreover, because the method makes it possible to evaluate changes as

small as 1%–2%, it can also be used to evaluate larger changes in porosity.

6. CONCLUSIONS

This paper introduces a thresholding method that considered the partial volume effect. The method was used to calculate the porosity of packed glass beads using X-ray CT images. The effects of the scanning conditions on the segmentation results were also examined. The same thresholding method was successfully used to calculate the porosity of Berea sandstone using X-ray CT images.

We focused on the variations in porosity in the same porous materials. Biogrouted and ungrouted packings of glass beads were measured using X-ray CT, and their porosities were evaluated using the thresholding method. The same method allows us to evaluate small changes in porosity with high accuracy.

REFERENCES

Abell, A.B., Willis, K.L., Lange, D.A., 1999. Mercury intrusion porosimetry and image analysis of cement-based materials. Journal of Colloid and Interface Science 211, 39–44. doi:10.1006/jcis.1998.5986.

Choi, H.S., Haynor, D.R., Kim, Y.M., 1991. Partial volume tissue classification of multichannel magnetic-resonance images: a mixel model. IEEE Transactions on Medical Imaging 10 (3), 395–407. doi:10.1109/42.97590.

Denoyel, R., Thommes, M. (Eds.), 2006. Meso- and Macropore Analysis: Mercury porosimetry and Alternative Liquid Penetration Techniques (Special Issue). Particle and Particle Systems Characterization 23 (1).

Fukuda, D., Nara, Y., Mori, D., Kaneko, K., 2010. Sealing behavior of fracture in cementitious material with micro-focus X-ray CT. In: Alshibli, K. A., Reed, A. H. (Eds.), Advances in Computed Tomography for Geomaterials (GeoX 2010, New Orleans, USA), ISTE, London, pp. 148–155.

Hart, D.J., Wang, H.F., 1995. Laboratory measurements of complete set of poroelastic moduli for Berea sandstone and Indiana limestone. Journal of Geophysical Research, 100 (B9), 17741–17751. doi:10.1029/95JB01242.

Jaeger, J.C., Cook, N.G.W., Zimmerman, R.W., 2007. Fundamentals of Rock Mechanics, 4th edn., Blackwell, Malden, MA, 475pp.

Kageyama, Y., Nishida, M., 2004. Lineament detection from land cover information in mixels using Landsat-TM data. Electrical Engineering of Japan 148 (4), 65–73. doi:10.1002/eej.10342.

Kak, A.C., Slaney, M., 1988. Principles of Computerized Tomographic Imaging, SIAM, New York, 327pp.

Kato, M., Takahashi, M., Kaneko, K., 2008. Estimation of rock porosity using X-ray CT image. Geoinformatics 19 (2), 132–133 [in Japanese with English title].

Kato, M., Kobayashi, Y., Kawasaki, S., Kaneko, K., 2009. Extraction of porosity change of geomaterials using X-ray CT images. Geoinformatics 20 (2), 112-113 [in Japanese with English title].

Kawaragi, C., Yoneda, T., Sato, T., Kaneko, K., 2009. Microstructure of saturated bentonites characterized by X-ray CT observations. Engineering Geology 106 (1-2),

51–57. doi:10.1016/j.enggeo.2009.02.013.
Kawasaki, S., Murao, A., Hiroyoshi, N., Tsunekawa M., Kaneko K., 2006. Fundamental study on novel grout cementing due to microbial metabolism. Journal of the Japan Society of Engineering Geology 47(1), 2–12 [in Japanese with English abstract]. doi:10.5110/jjseg.47.2.
Ketcham, R.A., Carlson, W.D., 2001. Acquisition, optimization and interpretation of X-ray computed tomographic imagery: applications to the geosciences. Computers & Geosciences 27 (4), 381–400. doi:10.1016/S0098-3004(00)00116-3.
Kim, J.S., Singh, V., Lee, J.K., Lerch, J., Ad-Dab'bagh, Y., MacDonald, D., Lee, M.L., Kim, S.I., Evans, A.C., 2005. Automated 3-D extraction and evaluation of the inner and outer cortical surfaces using a Laplacian map and partial volume effect classification. NeuroImage 27 (1), 210–221. doi:10.1016/j.neuroimage.2005.03.036.
Kitamoto, A., 1999. A maximum likelihood thresholding method considering the effect of mixels. Technical Report of IEICE PRMU99-166, 7–14 [in Japanese with English abstract].
Kitamoto, A., 2000. The moments of the mixel distribution and its application to statistical image classification. In: Advances in Pattern Recognition (Proceedings of the Joint IAPR International Workshops SSPR 2000 and SPR 2000, Alicante, Spain), Published in: Lecture Notes in Computer Science, Springer, Berlin / Heidelberg, Vol. 1876, pp. 521–531. doi:10.1007/3-540-44522-6.
Kitamoto, A., Takagi, M., 1998a. Estimating the area properties of mixels using mixture density estimation with mixel densities. Denshi Joho Tsushin Gakkai Ronbunshi (Transactions of IEICE) J81-D-II (6), 1160–1172 [in Japanese with title and diagram captions in English].
Kitamoto, A., Takagi, M., 1998b. Image classification method using area proportion density that reflects the internal structure of mixels. Denshi Joho Tsushin Gakkai Ronbunshi (Transactions of IEICE) J81-D-II (11), 2582–2597 [in Japanese with title and diagram captions in English].
Kitamoto, A. Takagi, M., 1999. Image classification using probabilistic models that reflect the internal structure of mixels. Pattern Analysis & Applications 2 (1), 31–43. doi:10.1007/s100440050012.
Kitamoto, A., Takagi, M., 2000. The area proportion distribution-relationship with the internal structure of mixels and its application to image classification. Systems and Computers in Japan 31 (5), 57–76. doi:10.1002/(SICI)1520-684X(200005).
Kittler, J., Illingworth, J., 1986. Minimum error thresholding. Pattern Recognition 19 (1), 41–47. doi:10.1016/0031-3203(86)90030-0.
Kobayashi, Y., Kawasaki, S., Kato, M., Mukunoki, T., Kaneko, K. (2009), Applicability of a method for evaluation of porosity to biogrouted geomaterials, Journal of MMIJ, 125 (10, 11), 540–546 [in Japanese with English abstract].
Kobayashi, Y., Kawasaki, S., Kato, M., Mukunoki, T., Kaneko, K., 2010. Evaluation of porosity in geomaterials treated with biogrout considering partial volume effect. In: Alshibli, K. A., Reed, A. H. (Eds.), Advances in Computed Tomography for Geomaterials (GeoX 2010, New Orleans, USA), ISTE, London, pp. 287–294.
Kurita, T., Otsu, N., Abdelmalek, N., 1992. Maximum likelihood thresholding based on population mixture models. Pattern Recognition 25 (10), 1231–1240. doi:10.1016/0031-3203(92)90024-D.

Lo, T.-W., Coyner, K.B., Toksoz, M.N., 1986. Experimental determination of elastic anisotropy of Berea sandstone, Chicopee shale, and Chelmsford granite. Geophysics, 51 (1), 164–171. doi:10.1190/1.1442029.
Menéndez, B., Zhu, W., Wong, T.-f., 1996. Micromechanics of brittle faulting and cataclastic flow in Berea sandstone. Journal of Structural Geology, 18, 1–16. doi:10.1016/0191-8141(95)00076-P
Miwa, S., 1981. Introduction to Powder Technology, Nikkan Kougyou Shinbunsha, Tokyo, Japan, 245pp. [in Japanese]
Ogata, S., Kawasaki, S., N. Hiroyoshi, N., Tsunekawa, M., Kaneko, K., Terajima, R., 2010. Temperature dependence of calcium carbonate precipitation for biogrout. In: Vrkljan, I. (Ed.), Rock Engineering in Difficult Ground Conditions: Soft rocks and Karst (EUROCK 2009, Dubrovnik, Cavtat, Croatia), Taylor & Francis Group, London, pp. 339–344.
Oh, W., Lindquist, W.B., 1999. Image thresholding by indicator kriging. IEEE Transactions on Pattern Analysis and Machine Intelligence 21 (7), 590–602. doi:10.1109/34.777370.
Okamoto, K., Fukuhara, M., 1996. Estimation of paddy field area using the area ratio of categories in each mixel of Landsat TM. International Journal of Remote Sensing 17 (9), 1735–1749. doi:10.1080/01431169608948736.
Otsu, N., 1979. A threshold selection method from gray-level histograms. IEEE Transactions on Systems, Man, and Cybernetics SMC-9 (1), 62-66. doi:10.1109/TSMC.1979.4310076.
Schembre, J.M., Kovscek, A.R., 2003. A technique for measuring two-phase relative permeability in porous media via X-ray CT measurements, Journal of Petroleum Science and Engineering, 39 (1-2), 159-174. doi:10.1016/S0920-4105(03)00046-9.
Sekita, I., Kurita, T., Otsu, N., Abdelmalek, N.N., 1995. Thresholding methods considering the quantization error of an image. Denshi Joho Tsushin Gakkai Ronbunshi (Transactions of IEICE) J78-D-II (12), 1806-1812 [in Japanese with title and diagram captions in English].
Shattuck, D.W., Sandor-Leahy, S.R., Schaper, K.A., Rottenberg, D.A., Leahy, R.M., 2001. Magnetic resonance image tissue classification using a partial volume model. NeuroImage, 13 (5), 856–876, doi:10.1006/nimg.2000.0730.
Shoji, H., 2008. Mechanical properties of soil specimens improved by biogrout. Unpublished Graduation Thesis, Hokkaido University, Sapporo, 82pp. [in Japanese with English abstract]
Takahashi, M., Kato, M., Urushimatsu, Y., Park, H., 2009. Quantification of 3 dimensional pore geometry in porous rock and application to hydraulic pressure dependency of Berea sandstone. Journal of the Japan Society of Engineering Geology 50 (5), 280–288 [in Japanese with English abstract].
Tohka, J., Zijdenbos, A., Evans, A., 2004. Fast and robust parameter estimation for statistical partial volume models in brain MRI. NeuroImage 23 (1), 84–97. doi:10.1016/j.neuroimage.2004.05.007.
Yamanaka, H., Kawasaki, S., Kato, M., Mukunoki, T., Kaneko, K., 2011. Segmentation of internal structure of two-phase materials using micro-focus X-ray CT. Jiban Kogaku Janaru (Japanese Geotechnical Journal) 6 (2), 273–284 [in Japanese with English abstract]. doi:10.3208/jgs.6.273.

Zhang, J., Wong, T.-f., Yanagidani, T., Davis, D.M., 1990. Pressure induced microcracking and grain crushing in Berea and Boise sandstones: acoustic emission and quantitative microscopy measurements. Mechanics of Materials, 9, 1–15. doi:10.1016/0167-6636(90)90026-C.